Solid Earth Discuss., 4, 707–744, 2012
www.solid-earth-discuss.net/4/707/2012/
doi:10.5194/sed-4-707-2012

Solid Earth
Discussions

Using open sidewalls for modelling self-consistent lithosphere subduction dynamics

M. Chertova, T. Geenen, A. van den Berg, and W. Spakman

Utrecht University, Utrecht, The Netherlands

Received: 11 May 2012 – Accepted: 13 May 2012 – Published: 18 June 2012

Correspondence to: M. Chertova (m.v.chertova@uu.nl)

Published by Copernicus Publications on behalf of the European Geosciences Union.

Abstract

Subduction modelling in regional model domains, in 2-D or 3-D, is commonly done using closed, vertical boundaries. In this paper we investigate the merits of using open boundaries for 2-D modelling of lithosphere subduction but with implication for 3-D modelling. Open sidewalls allow for lateral in- and outflow consistent with the internal dynamics of the model and may simulate the real-mantle environment of subduction much better than closed boundaries, which induce return flows. Our experiments are focused on using open and closed (free-slip) sidewalls while comparing results for two model aspect ratios of 3:1 and 6:1. Slab buoyancy driven subduction with open boundaries immediately develops into strong rollback with high trench retreat velocities. Mantle asthenosphere flow forced by rollback is predominantly laminar and facilitated by the open boundaries. In contrast, free-slip sidewalls proof restrictive on subduction rollback evolution unless the lithosphere plates are allowed to move away from the sidewalls. This, however, initiates return flows pushing both plates toward the subduction zone speeding up subduction. Increasing the aspect ratio to 6:1 does not change the overall flow pattern when using open sidewalls. Again, in contrast, for free-slip boundaries, the slab evolution does change with respect to the 3:1 aspect ratio and does not resemble the 6:1 evolution obtained with open boundaries. We notice a general drop in the amplitude of mantle flow when changing to the 6:1 aspect ratio, which is caused by the increasing shear friction between mantle and lithosphere while the driving slab buoyancy is the same. Based on energy-dissipation arguments we applied a flow speed scaling to convert between flow fields of different model aspect ratios. This proved succesful for the open boundary model. We have also investigated the effect of far-field stress conditions in our open boundary models. Applying realistic normal stress conditions to the strong part of the overriding plate we show that “intra-plate” stresses control subduction dynamics resulting in slab roll-back, stationary or advancing subduction. We conclude that open boundaries are to be preferred for modelling subduction evolution (rollback, stationary or advancing). The relative independence of model aspect ratio

avoids the need to place sidewalls at large distance and allows to focus all computational resources on a smaller modelling domain. Open boundaries simulate the natural subduction environment better and avoid the adverse effects (e.g. forced return flows) of free-slip boundaries.

1 Introduction

In the past decades, numerical modelling of lithosphere subduction has advanced considerably by incorporating coupling between plates, between plates and mantle, and by incorporating the complexity of detailed subduction zone processes (see Gerya, 2011, for a review and references therein). Up to now modelling of regional subduction evolution is still being performed within spatially bound modelling domains in 2-D or 3-D (e.g. Quinquis et al., 2011, Jadamec and Billen 2012). The limited spatial domain particularly requires prescribing boundary conditions on the vertical sidewalls of the domain. These conditions are an important influence on the development of the model interior (Quinquis et al., 2011). The usual attempt to reduce possible sidewall influence is by moving these far away from where subduction occurs by using a sufficiently large aspect ratio of model length to depth (e.g. Cizkova et al., 2012). Boundary conditions on the vertical sidewalls can be no-slip (no flow at the boundary), free-slip (impermeable; no flow through the boundary), or "open" to some particular form of through-flow. Free-slip is the most commonly used boundary condition while open boundaries have been mostly limited to completely prescribed in- and out-flow (e.g. Van Hunen et al., 2000; Baes et al., 2010; Quinquis et al., 2011), or periodic conditions requiring that the through-flow at one side is the mirror image of through-flow on the other (e.g. Enns et al., 2004; Capitanio et al., 2010). Open boundaries for which the horizontal in- and outflow are defined by a "fully internally developed flow" , have hardly been used and are the main topic of the present paper. Such open boundaries basically prescribe a hydrostatic pressure condition on the boundary preventing the model to collapse while horizontal in and out-flow is free, in the sense that it is driven by the internal dynamics

SED
4, 707–744, 2012

and the usual condition of incompressible flow. Among the range of boundary conditions used, open boundaries may fit best to real-mantle flow conditions surrounding subduction zones. We know of only one example (Quinteros et al., 2010) of Eulerian modelling with non-periodic open boundaries.

Our aim in this paper is to investigate the benefits of using open boundaries as compared to using closed (free-slip) conditions at the sidewalls of a two-dimensional (2-D) model domain. We focus on modelling self-consistent subduction driven by internal buoyancy and boundary stress conditions only, i.e. no kinematics are prescribed, in the presence of an overriding (oceanic) plate. Our focus will be on the effects of boundary conditions and model aspect ratios on subduction and mantle evolution. As our results show strong differences between using free-slip and open boundaries, we are considering first order aspects only. Our results also show that with open sidewalls increasing the model aspect ratio does not change the overall evolution of subduction and mantle flow. In contrast, closed boundaries keep influencing the evolution of the model even for large model size of 6000 km by 1000 km. The primary reason is that closed sidewalls basically cause return flows from both sides towards the centre of the model which feeds back artificially into the evolving the subduction process. We expect this also to hold for 3-D models despite the larger degree of freedom to develop lateral flow.

2 Model description

2.1 Model setup

We model self-consistent, internally driven, lithosphere subduction in the presence of an overriding plate in a 2-dimensional Cartesian geometry. Our main focus is on how distinctly different boundary conditions on the two sidewalls, open versus impermeable boundaries, affect subduction evolution. We will also investigate whether increasing the aspect ratio of the model domain from 3:1(3000 km × 1000 km) to

6:1(6000 km × 1000 km) is of influence, particularly, in reducing any observed adverse effect of boundary conditions.

The boundary condition for the top and the bottom of the box is free-slip (impermeable). The surface condition will not allow for modelling topography but, as discussed later in Sect. 2.3, we impose a low-viscosity top layer of crust, which will partly compensate for the impermeability condition by allowing for lithosphere bending prior to subduction. For the right and left sides different types of boundary conditions were implemented: open boundaries or free slip boundaries. Open boundaries are implemented by constraining zero tangential velocity on the boundary and by imposing a lithostatic pressure condition for the normal stress on the boundary: $\sigma_n = P_{\text{lith}}$.

This allows for horizontal in- and outflow purely driven by the internal dynamics of the model. The pressure condition prevents that the model collapses. As discussed in the introduction, open boundaries are hardly used in subduction modelling, but provide a more natural simulation of the mantle outside the model domain than the more common free-slip, impermeable boundary conditions. The free-slip condition prevents material transport through the boundary and forces the flow parallel to the boundary.

2.2 Governing equations

We adopt the Boussinesq approximation comprising three coupled equations of mass conservation of an incompressible viscous fluid, $\nabla \cdot u = 0$ the Stokes equation describing force balance, $-\nabla P + \nabla \cdot \tau = f(\rho)$ and the heat equation which here only takes into acount heat diffusion and heat advection: $\rho c_p \frac{dT}{dt} - \nabla \cdot (\kappa \nabla T) = 0$ (for explanation of symbols see Table 1). This system of equations is solved numerically using the finite element modelling package SEPRAN (Segal and Praagman, 2005). The mesh element size varies from 1.5 km in the trench region to 20 km at the bottom of the model. Advection of the low viscosity material defining the crust and wedge is performed with a Lagrangian tracer technique where material properties are defined on tracers that are advected with the flow. Tracers are distributed initially only over the top 200 km of our domain where we use them to define rheological properties for a low viscosity top layer and wedge.

2.3 Rheological model

A composite rheology is used, which comprises dislocation and diffusion creep and a viscosity maximum $\eta_{\max}$. The effective viscosity η_{eff} is determined as: $\frac{1}{\eta_{\text{eff}}} = \frac{1}{\eta_{\text{diff}}} + \frac{1}{\eta_{\text{disl}}} + \frac{1}{\eta_{\max}}$ with $\eta_{\max} = 10^{24}$ Pas limiting the effective viscosity in the coldest parts of the lithosphere, with the viscosity due to diffusion creep,

$$\eta_{\text{diff}} = \mu A_{\text{diff}}^{-1} \left(\frac{b}{d}\right)^{-m} \exp\left(\frac{E_{\text{diff}} + pV_{\text{diff}}}{RT}\right) \tag{1}$$

and dislocation (power law) creep

$$\eta_{\text{disl}} = \mu A_{\text{disl}}^{-\frac{1}{n}} \dot{\epsilon}^{\frac{1-n}{n}} \exp\left(\frac{E_{\text{disl}} + pV_{\text{disl}}}{nRT}\right), \tag{2}$$

where $\dot{\epsilon}$ is the second invariant of the strain-rate tensor, A_{diff}, A_{dis} are diffusion and dislocation creep viscosity prefactors, μ is the shear modulus, b is Burgers vector, d is the grain size, m is the grain size exponent, $V_{\text{diff,dis}}$ and $E_{\text{diff,dis}}$ are activation volume and activation energy for diffusion and dislocation creep respectively, P is the lithostatic pressure and T-temperature (Table 1). Parameters are taken for wet olivine (Karato et al., 2001), values are given in Table 1. Activation volumes, energy and grain size are the same as determined in seismic studies and postglacial rebound estimations of upper mantle and astenosphere viscosities (Kaufmann, 2000; Burgmann and Dresen, 2008; Simmons et al., 2006).

2.4 First order phase changes

Our models include the two major phase transitions at approximately 410 km and 660 km depth. The values of the Clapeyron slope and density contrast are given in Table 1. These parameters are chosen following Billen, 2010. The 410 km phase change

SED
4, 707–744, 2012

contributes to the buoyancy force and increases slab pull. The phase change at 660 km has a positive buoyancy effect on cool material resisting slab penetration to the deeper mantle. We ignore thermal effects associated with the phase changes. Phase transitions are parameterized in the model with the phase-transition function:

$$\Gamma_k = \frac{1}{2}\left(1 + \sin\left(\frac{\pi z_{\text{diff}}}{w}\right)\right), \tag{3}$$

where $z_{\text{diff}} = z - z_{\text{tr}} - \gamma_k \cdot (T - T_{\text{tr}})$, w is half-width of kth transition zone, z_{tr} and T_{tr} are the reference depth and temperature of the phase transition, respectively, γ_k is the Clapeyrone slope, T is the temperature (Cristensen and Yuen 1985; van Hunen 2001).

2.5 The starting configuration leading to the initial buoyancy field

To enable internally-driven subduction, first an initial buoyancy distribution is created by kinematically forced subduction (10 cm yr^{-1}) along an arc-shaped fault extending from 0 to 300 km depth. The lithosphere temperature distribution prior to subduction is determined from the equation of cooling of a semi-infinite halfspace (Turcotte and Schubert, 2002) for a lithosphere age of 100 My. Boundary temperature conditions are $T = 273$ K at the surface, $T = 2000$ K at the bottom. On the side boundaries we prescribe a stationary temperature profile during the subduction process. This also defines the thermal structure of the overriding plate.

We implemented a 10 km thick weak layer (10^{19} Pas) on the top of the subducted plate (Han and Gurnis, 1999; Manea and Gurnis, 2007; Cizkova et al., 2007; Behounkova and Cizkova, 2008; Babeyko and Sobolev, 2008; Quinteros et al., 2010). This mimics a subduction channel and proves sufficient for initiating and maintaining subduction in our modelling. An accretionary wedge of weak crust is formed above the subduction zone and has the advantage to prevent artificial rheological coupling between the subducting and overriding plates. The presence/absence of the accretionary wedge only leads to small differences in dip angle and stress field of the trench zone and does not affect the overall subducting slab evolution for the boundary conditions we consider in our models, we conclude from various tests. The focus in our paper is on the large-scale evolution of the subduction system linked to various boundary conditions and aspect ratios of the model domain rather than on the detailed evolution of the plate boundary region.

Figure 1a shows the initial rheology field for the model with open boundaries. In the oldest part of the slab both dislocation and diffusion creep give high viscosity values which are limited here by $\eta_{\max} = 10^{24}$ Pas. In the asthenosphere viscosity decreases to values of 10^{19} Pas, below which it increases to 0.5×10^{21} Pas in the transition zone and to 10^{22} Pas at the top of the lower mantle. The tip of the slab in this initial configuration shows thickening due to mantle resistance, which is also visible in the τ_{22} component of the stress distribution (Fig. 2). The starting configuration, rheology and flow field, using free-slip sidewalls is illustrated in Fig. 1b. The two types of boundary conditions, closed or open, lead to a different internal flow field and velocity gradient field on which viscosity depends. Therefore, the starting configuration, particularly the viscosity field, depends on the boundary conditions used and is different when using open sidewalls or free-slip sidewalls.

The dominant deformation mechanisms acting in the initial model are shown in Fig. 3. Diffusion creep(red) is dominant below the asthenosphere and away from the slab, where dislocation creep is active. Small red regions beneath the overriding plate correspond to low strain rate regions. In the core of the slab and overriding plate the viscosity is limited to $\eta_{\max} = 10^{24}$ Pas. The low viscosity crustal layer and accretionary wedge are shown in yellow.

3 Results of numerical modelling

We first focus on models with open versus closed boundary conditions and on model domains with different aspect ratio. This concerns end-member models driven by slab buoyancy only. Subsequently, we incorporate far-field effects additionally constraining the motion of the upper plate. These are imposed by means of a normal-stress

SED
4, 707–744, 2012

boundary condition (τ_{11}) acting on the strong lithosphere at both sidewalls. This condition allows investigating stationary or advancing subduction using open boundaries of which we will show several results. After the initial 3.5 My of kinematically forced subduction has provided an initial buoyancy configuration as discussed in Sect. 2.5, the forcing is removed and the internal dynamics take over in driving subduction. We label the models using "O" to denote open, "C" for closed, "R" for "spreading ridge", and "3" and "6" to denote aspect ratio 3:1, and 6:1, respectively.

3.1 Open versus closed vertical boundaries and aspect ratio of 3:1

For the models with aspect ratio 3:1, Fig. 4 shows the velocity field and rheology structure of four models (columns) at 2 My intervals (rows) and with different boundary conditions on the left and right sidewalls.

Figure 4a depicts the evolution of the model OO3 with two open side boundaries. During the initial stage, about 3.5–4 My from the beginning of the subduction, we observe a strong horizontal flow associated with the subducting plate. This flow pattern bends into the subduction zone following the slab. During this early stage, the upper plate does not move appreciably. However, in the next 2 My slab rollback starts and forces an overall left directed horizontal flow of the upper plate and in its underlying asthenosphere. The subducting plate is still being pulled into the subduction zone, but with decreasing speed. Around 5.5 My the slab reaches the base of the upper mantle and further subduction meets resistance due to slab interaction with the 660 km phase transition and with the increased mantle viscosities of the lower mantle. This is followed by the onset of increased slab retreat. The overriding plate attains velocities of 10–15 cm yr^{-1}, while the advance velocity of the subducting plate drops down to small values (2–3 cm yr^{-1}). During the subsequent subduction evolution we observe strong horizontal left-directed laminar flow concentrated in the asthenosphere and characterized by low viscosity (red colors) in Fig. 4a. This development proofs to be characteristic for models with open boundaries and driven by slab buoyancy only.

SED
4, 707–744, 2012

Figure 4b illustrates the evolution of a model with a closed left and an open right boundary (CO_3). The closed left boundary effectively fixes the upper plate to the side. During the whole evolution of the subduction process we observe a low velocity magnitude (more than 10 times lower than for model OO3). As a result also the viscosity structure is different from model OO3. The minimum viscosities for the asthenosphere, corresponding to lower strain rate, are higher(around 1 order of magnitude), and the rheological width of the asthenosphere is reduced considerably. After the slab reaches the top of the lower mantle we observe no more trench retreat and the velocity magnitude drops to almost zero. This occurs because the left part of the domain effectively forms a closed volume at this stage in which the slab is blocking flow to the right part of the domain. This is a pure 2-D effect. In 3-D modelling flow is developing at the (open) lateral edge of the slab, which allows material to move away sideways from below the slab (e.g. M. OzBench et al., 2008, Stegman et al., 2010, Funiciello et al., 2003, Piromallo et al., 2006). Figure 4c shows the evolution of a model with closed boundaries on both the left and right sides. The closed left boundary again fixes the upper plate, but at the closed right boundary a "spreading ridge" is allowed to develop in the upper right corner of the model (CCR3) (e.g. Enns et al., 2004). The "spreading ridge" enables the lithosphere plate to separate from the vertical boundary by allowing "hot" asthenosphere to flow upward. This facilitates more free lateral movement of the upper plate and is initiated by defining a warm weak zone at the boundary in the initial temperature field. For this model we also observe much lower flow magnitudes (1 $cm\,yr^{-1}$ after arriving of the slab at the 660 km boundary) compared to OO3 and, correspondingly, a different evolution of the viscosity structure. The slab behaviour and trench rollback are similar to the model CO_3 except one difference: in model CCR3 a gap between the subducted slab and the overriding plate forms. This gap is filled with asthenosphere material as can be seen from Fig. 4c mimicking the formation of a back-arc basin. While in model CO_3 the open right boundary allows for modest inflow of asthenosphere material with flow speeds comparable to the overlying the upper plate, this does not happen in model CCR3. When the slab reaches the bottom of the upper mantle material exchange with the left part of the model is mostly blocked as in model CO_3. However, the closed right boundary now forces an asthenospheric return flow in response to slab rollback with larger magnitude than the “free” upper plate can attain. As a consequence back-arc basin opening develops.

Lastly, Fig. 4d illustrates the evolution of a model with closed boundaries but with “spreading ridges” in both upper corners (CRCR3) allowing both lithosphere plates to separate from the sidewall. Although the 3:1 aspect ratio was wide enough to enable the development of large horizontal flow in the model with open boundaries OO3, this proves more complicated for model CRCR3 with closed boundaries in combination with ”free” plates. We observe strong boundary influence on the motion of the plates and the flow field around the slab. This flow is directed upward close to the vertical boundaries and pushes both plates toward the subduction zone. For this model with closed boundaries and “free” plates we observe a lower velocity for the overriding plate (5–6 $\mathrm{cm\,yr^{-1}}$ on average) compared to OO3 model and higher viscosities for the asthenosphere. The rollback process develops slower than in model OO3, but the evolution of the slab and the overriding plate as well as the evolution of rollback are more similar to the model OO3 than to models CO_3 and CCR3. No back-arc basin evolves in model CRCR3. The reason is that, while rolling back, the subducting plate is still advancing as can be inferred from the slab reaching larger depths, which reduces the sinking velocity and no gap appears between upper and lower plate.

3.2 Comparison of the end-member (OO3 and CRCR3) models

From the velocity vector plots, Fig. 4a and d clear difference in the magnitude of flow between the models OO3 and CRCR3 is observed, illustrating the strong impact of the choice of boundary conditions. Despite the smaller rollback rate, we observe higher horizontal velocities of the subducting plate for the closed boundary case CRCR3, as a result of the ridge push from the “spreading centers” at both sides of the subduction zone. The flow patterns in both models are distinctly different: in model OO3 a strong lateral flow is created by slab rollback pushing material out of the model domain. This sets up a high-magnitude "channel flow" in the low-viscous asthenosphere (peak velocity 16.5 cm yr^{-1}). For the model with closed boundaries the flow aligns with the slab and splits up into two cells with upward limbs near the side boundaries.

Besides the differences in magnitude of the velocity field, we notice also a difference in rheological structure. For model OO3, at the start of the subduction process, the minimum viscosities in the asthenosphere are around 10^{19} Pas. For model CRCR3 these are by one order of magnitude larger. These viscosity values decrease with time, but the asthenosphere in model CRCR3 stays narrower than in model OO3. This feature is related to the dominant deformation mechanism in the asthenosphere, which is strain-rate dependent dislocation creep (Fig. 2). Overall, viscosity values in model CRCR3 are larger during the entire subduction process.

The evolution of the subduction angle is also different between the two end member models OO3 and CRCR3: for model OO3 it gradually decreases while for model CRCR3 it increases with time. This is related to the large difference in the speed of trench retreat while the deep part of the slab is not moving backward. In OO3 this changes the average slab dip and subduction angle. In model CRCR3 the slab penetrates deeper into the lower mantle during the subduction process as a result of a smaller rate of trench retreat creating a steeper average subduction angle.

3.3 Comparison of models with different aspect ratios

One possible way to reduce the influence of the sidewalls conditions on the evolution of lithosphere subduction is to increase the width of the domain, but at increased cost of computations. To investigate this we increased the domain width to 6000 km doubling the aspect ratio to 6:1. Figure 5 shows results for models with open and closed sidewalls with "spreading ridges", labelled OO6 and CRCR6 respectively. The flow fields are illustrated here by plotting the instantaneous streamlines, which show again significant differences between both models.

For model CRCR6 the velocity magnitude is smaller (after 14 My of subduction maximum velocities are 6.5 and 3.5 cm yr^{-1} for OO6 and CRCR6 respectively) and the

SED
4, 707–744, 2012

lowest viscosities beneath the slab are at least 10 times higher than in model OO6. Similar observations were made for model OO3 and CRCR3. Figure 6 shows vertical velocity profiles of computed at different distances from the left side of the models OO6 and CRCR6 after 14 My from the beginning of the subduction process. These profiles clearly illustrate the difference between flow regimes for these two models. Particularly for model OO6 it illustrates the channel flow regime of the asthenosphere as well as plate-like behavior (van den Berg et al., 1991; Turcotte and Schubert, 2002). Flow velocities in the asthenosphere channel are much higher for the “open boundary” case, while plate velocities are higher for the “closed boundary” case with “free” plates. Apparently the slab rollback process produces a significant pressure gradient that drives laminar flow in the astenosphere. In contrast, model CRCR3 shows weaker slab rollback associated with only little asthenosphere return flow from the “far-field”. Flow patterns around the slab in model CRCR6 are different from those in OO6 due to the different retreat velocity and the return flow resulting from the closed sidewalls. In model OO6 with “open boundaries” streamlines cross the slab and leave the domain, illustrating that the boundary does not obstruct the slab migration. For the “closed boundary” model CRCR6 the flow tends to follow the slab then deflects downward and forms closed streamlines. In this model the return flow in the upwelling limbs of the convective cells at both sides contributes to the convergence of the two plates, which puts the subduction channel under lateral compression. For models with a thin crustal weak layer this lateral compression may lead to locking between the subducting and overriding plates. We conclude that using a larger aspect ratio does not reduce the differences in subduction evolution and overall flow field between models with open and closed boundaries.

3.4 Rollback velocity and the overall magnitude of flow speed

The almost uniform velocities within the subducting and overriding plates allow us to focus on the speed of slab rollback measured from the trench position through time. Figure 7 shows the speed of rollback for the models with aspect ratio 3:1 and 6:1 and

SED
4, 707–744, 2012

different side boundary conditions. For the models OO3 and CRCR3, yellow and green curves respectively, Fig. 7 shows the difference between rollback speed amounting to a factor of nearly 3 after 8 My of subduction. We observe common trends in the development of the rollback speed: (1) until the slab reaches the 410-km phase change, the speed of rollback increases with a factor of 2; (2) next subduction rollback slows down until the slab reaches the 660-km phase change and the top of the lower mantle; (3) Lastly, slab rollback continues while the tip of the slab is "hanging" in the highly viscous lower mantle, i.e. without an increase in the penetration depth of the slab. For model OO3 we observe an increase in rollback speed during this last stage of subduction, which is linked to the trench coming closer to the open boundary. This latter effect is not observed in the 1:6 aspect ratio model OO6 (Fig. 7, blue curve). For model OO6 the rollback speed stabilizes after the slab tip gets stuck in the high viscosity lower mantle. Model CRCR6 (Fig. 7, red curve) with "free" plates has a particular evolution from initially no rollback to strongly increasing speeds peaking around 8 My. This evolution is dominated by the detaching of the overriding plate from the right boundary while low-viscosity mantle material starts filling the gap. Figure 7 demonstrates in a different way the large effects of boundary conditions, open versus closed, which cannot be reduced using larger aspect ratio. Another large difference between the results obtained for different aspect ratios of the modelling domain concerns the overall magnitude of flow speed of the lithosphere plates, subduction speed and mantle flow. Figure 7 shows that for the 3:1 model with open boundaries the average rollback speed is roughly 15 $\mathrm{cm\,yr^{-1}}$ whereas for the model with aspect ratio 6:1 it is around 5 $\mathrm{cm\,yr^{-1}}$. A similar reduction in flow speed characterizes the mantle flow. In all aspect-ratio cases the initial driving slab buoyancy is the same. These flow speed reductions can be tied to the longer length of the lithosphere plates in the 6:1 models causing a longer sublithospheric frictional shear zone where a significant part of the mechanical energy of the system is dissipated. For models with open boundaries we can, in an approximate way, compensate for the reduced (increased) effect of viscous dissipation in the 3:1 (6:1) models by a scaling relation applied to the velocity field and which accounts for

SED
4, 707–744, 2012

the effect of additional viscous dissipation in an extended computational domain. To determine this velocity scaling, we investigated aspect ratios of 3:1, 4:1, 5:1 and 6:1, where an aspect ratio of 6:1 would correspond to the ocean halfwidth of 3000 km of the subducting plate. The scaling procedure is explained in more details in Appendix A. This scaling procedure has been applied during the computation of the OO3 model to approximate flow speed results as observed for the 6:1 aspect ratio. Figure 8 shows scaled rollback velocities of the OO3 model together with original (unscaled) velocities for both the OO3 and OO6 models. These results illustrate the feasibility of approximate "upscaling" the numerical results for a larger domain. For the models with closed boundaries we cannot apply velocity scaling due to lateral variations of the flow close to the side boundaries. For models with closed boundaries not only the velocity magnitude but also the flow pattern is changing with decreasing/increasing domain size. In this case comparison of the subduction dynamics in models with different aspect ratio is not meaningful.

3.5 Constraining the motion of the lithosphere plates

In the open boundary models OO3 and OO6 the motion of the subducting and overriding plate are entirely controlled by the buoyancy of the subducting slab. We invariably observe (relatively fast) slab rollback in these models whereas on Earth not all subduction zones show strong rollback and advancing trenches are also proposed (e.g. Funiciello et al., 2008; Schellart et al., 2008). OO3 and OO6 are in fact end-member models as on Earth the global coupling between plates may impose "far-field" control on the velocity of both overriding and subducting plate. We devised a number of experiments to investigate the combination of far-field control and local slab buoyancy on the evolution of subduction using various boundary conditions in combination with open boundaries.

As a first open-boundary experiment we impose "far-field" control by just fixing the upper plate to the right boundary (model OOF3). We compare this to a model in which the left boundary is open while the right boundary is entirely closed (model OC3). The latter experiment is similar to that of Quinteros et al. (2010) who also use a single

SED
4, 707–744, 2012

open vertical boundary in their numerical modelling of free slab movement. Results are presented in Figure 9 showing snapshots of the effective viscosity field at 5 My intervals. The initial models at 3.5 My are similar apart from the fact that model OOF3 already shows clear laminar flow field in the asthenosphere under the overriding plate as facilitated by the open boundaries. During the next 5 My the flow fields are of comparable magnitude and differ mostly in the flow near the tip of the slab. The average slab dip develops different between the models and particularly when the slab reaches the transition zone the evolution of these models starts to diverge. For model OOF3, active subduction continues and the slab penetrates deeper under the overriding plate, although with a decreasing speed and with overall shape deformation (along dip buckling) as a result of the interaction with increased viscosities at depth. In the second model (OC3), the slab starts ”hanging” in the transition zone after 8 My of evolution, the dip angle increases and the slab tends to overturn. The position of the trench does not change with time. The flow field pattern to the right of the slab is completely different from that of model OOF3 with an open right boundary, which allows flow to leave the domain. In the second model OC3 the closed right boundary creates a circulation beneath the upper plate, which in combination with increasing viscosity below 660 km depth results in slab bending and folding.

To avoid prescribing plate velocities, we can devise a more general implementation of the far-field control by imposing an ”intra-plate” stress as a normal traction on the open boundary from the surface down to the base of the lithosphere. We applied this to the upper plate only. Some examples are presented here demonstrating that open boundaries in combination with “intra-plate” stress constraints can lead to strongly reduced slab rollback, (temporary) stationary subduction, or even advancing trenches as compared to the end-member “free” in/outflow models OO3 or OO6. We varied the applied “intra-plate” stress within reasonable limits for subduction zones (up to 52 MPa, Lithgow-Bertelloni and Guynn 2004). The results of the subduction models with different “intra-plate” stress values applied to the upper plate are presented in Figure 10 where a pull is exerted of 18 MPa (10A), 36 MPa (10B), and 52 MPa (10C) on the

SED
4, 707–744, 2012

Using open sidewalls

M. Chertova et al.

upper plate. With increasing value of the "intra-plate" stress we generally observe decreasing trench retreat. In more detail Fig. 10b shows an initial stage of stationary subduction, while Fig. 10c exhibits an initial phase of trench advance (to the right). These initial stages differ when as a result of a relatively short slab, the slab pull is still small and the pull on the upper plate is able to force stationary subduction or even slab advance. When the slab touches the 660-km boundary, there is a short episode of trench-stationary subduction, and after a few My trench retreat develops in the model (Funiciello et al., 2003). These results demonstrate that open boundaries are not restrictive on modelling rollback, stationary subduction or trench advance. In addition they again demonstrate the strong dependence of the evolution of trench motion and slab morphology on boundary conditions.

4 Discussion and conclusions

In this paper we set out to investigate the merits of using open sidewalls in 2-D modelling of subduction evolution as opposed to the more common impermeable free-slip condition. The particular implemented condition is to maintain lithostatic pressure at the boundaries while flow perpendicular to the boundary is free. The internal buoyancy in combination with normal stress conditions (pull/push) on the cross sectional area of the two lithosphere plates, is driving the flow. The absence of kinematic boundary conditions leads to a fully dynamically self-consistent evolution of the internal dynamics of the model. Simulating a weak upper crust (10 km thick, 10^{19} Pas) allowed for modelling continuous subduction without prescribing a particularly subduction channel geometry. We observed that changing the aspect ratio for models with open boundaries did not change the general flow patterns and subduction evolution, except for a general drop in flow speed amplitude for which we derived an approximate scaling procedure based on energy dissipation.

Discussion Paper | Discussion Paper | Discussion Paper | Discussion Paper |

SED

4, 707–744, 2012

Using open sidewalls

M. Chertova et al.

The modelling results obtained with the usual free slip condition (no horizontal flow) at the sidewalls are in strong contrast with the results obtained for open boundaries. We observed in all experiments a strongly deviating subduction evolution due to the unavoidable influence of return flows induced by the free slip boundaries and an order of magnitude difference in flow-dependent effective viscosity. If the lithosphere plates are allowed to move away from the boundary, which we implemented to relax the free slip condition on the motion of the plates, upward return flows at either boundary have an important adverse effect on subduction evolution, by forcing additional convergence, and model evolution in general. These effects could not be sufficiently reduced by taking a larger 6:1 aspect ratio (simulating the half-size of modern oceans), whereas for open boundaries it was found that the flow pattern and subduction evolution was basically independent of the aspect ratio. Also for closed sidewalls a general drop in flow speed was observed for larger aspect ratio models. However, the free slip boundaries prevented application of a useful scaling procedure.

Although our experiments are in 2-D, we do expect that using open boundaries in 3-D modelling of subduction evolution (e.g. Jadamec and Billen 2010; Piromallo et al., 2006; Van Hunen et al., 2011) may proof beneficial. In 3-D, flow patterns have larger degrees of freedom as toroidal flow can be excited, e.g., around slab edges, and perhaps remote free-slip boundaries may suffice, but as no material is allowed to leave or enter the model unfavourable effects of free-slip sidewalls cannot be excluded. Our primary conclusion is that open boundaries lead to the most natural boundary conditions for modelling realistic subduction evolution in 2-D and, we expect- 3-D as they avoid adverse effects of impenetrable “walls”, which are not present in Earth’s mantle either. Open boundaries can be combined with plate “push” or “pull” conditions, or kinematic conditions on the plates at the sidewalls, to simulate the far-field control of global plate tectonics. As also noted by Capitanio et al. (2010), and van Dinther et al. (2010), the tectonic style of subduction can be strongly controlled by far-field effects on both upper and lower plate. We notice a strong interaction between boundary conditions, internal flow field, and the viscosity field when using non-linear strain-rate dependent

SED
4, 707–744, 2012

rheology. For closed boundaries this feeds back into an effective viscosity of one order of magnitude larger in the asthenosphere, as compared to the asthenosphere viscosity in open-boundary models. Other advantages are the independence of the aspect ratio of the model domain, which allows for smaller models with increased resolution for modelling detail. An approximate scaling procedure can be used to tune the overall flow speed amplitude to levels consistent with the mantle outside the model domain as far as buoyancy inside the model would drive motions outside the model.

Appendix A

Scaling of the velocity for models with contrasting aspect ratios

We have shown that for models with open boundaries, the convective flow pattern is unaffected by the aspect ratio of the domain. However, due to the fact that the amount of viscous dissipation in the model interior decreases with decreasing aspect ratio we observe an increase in the magnitude of the flow velocity with decreasing aspect ratio of the model. We present an iterative method that allows us to scale the velocity of the small aspect ratio domain such that it is in agreement with larger aspect ratio models.

Figure A1 shows a snapshot of the dissipated power distribution

$$\Phi = \frac{1}{2}\dot{\epsilon}_{ij}\tau_{ij} \tag{A1}$$

where, $\dot{\epsilon}_{ij} = \partial_i u_j + \partial_j u_i$ and $\tau_{ij} = \eta\dot{\epsilon}_{ij}$. This figure illustrates that the dissipative power is concentrated within the slab and its surrounding in the central region of the domain. Other areas of significant dissipative power are located in the asthenosphere directly below the lithospheric plates towards the left and right hand boundary of the domain. The asthenospheric contribution to the dissipative power scales with the width of the domain.

Based on this configuration of the dissipative power we have applied an approximate scheme to scale the velocity for the effect of power dissipated in a "virtual" lateral

Discussion Paper | Discussion Paper | Discussion Paper | Discussion Paper |

SED

4, 707–744, 2012

Using open sidewalls

M. Chertova et al.

extension of the domain, schematically illustrated in Fig. A2. This way a uniform velocity scale factor is determined iteratively in the following steps:

1. Compute the volume integrated dissipative power for the interior domain labelled model 1 in Fig. A2, $P_{\text{in}}^{j} = \int_{V_{\text{in}}} \Phi^{(j)} dV$

2. Estimate the corresponding power, dissipated in the virtual extensions of the model, the regions labeled 1 and 2 in Fig. A2, dV This is done by uniform lateral extrapolation of the dissipation function profiles at the left and right hand side boundaries of the interior domain.

3. A velocity scaling factor is defined as:

$$f_j = \frac{(P_{\text{out}}^{(j)} + P^{(j)})}{P^{(1)}} \tag{A2}$$

4. Apply the scaling factor to the velocity field,

$$U^{(j+1)} = f_j U^{(j)} \tag{A3}$$

This procedure is repeated until convergence $|f_{j+1} - f_j| \leq 10^{-6}$, which is typically obtained within a few iterations. Despite of the fact that the values for the dissipation in the external regions represent less than 15–20 % of the total dissipation in the model, this iterative procedure leads to a significant reduction in the velocity field magnitude, due to the non-linear rheology.

The above-mentioned procedure was tested on several models with different aspect ratios. The results of the velocity scaling for these models are shown in Fig. A3. A where maximum velocity values in the domain for the model with aspect ratio 6 and scaled models with smaller aspect ratios are presented. The maximum velocities are typically observed in the asthenosphere below the overriding plate. The maximum evolution time is 18 My since, for the model with the smallest aspect ratio, the trench reaches the left boundary at this stage. The time-averaged difference in maximum velocities is 6 % for the 4:1 and 5:1 model and 14 % for 3:1. The maximum difference in velocity magnitude is, 20 % for the 5:1 model 30 % for the 4:1 model and 45 % for the 3:1 model. Without velocity scaling the difference in maximum velocities between 3:1 and 6:1 aspect ratio models after 12 My of evolution reaches approximately 70 %. and increases over time as illustrated in Fig. A3b.

Acknowledgements. This study is a contribution to the ESF EUROCORES project TOPO-EUROPE, particularly component TOPO-4D, of which our project is funded by NWO (Netherlands Organisation for Scientific Research) through grant 855.01.141. This work also contributes to ISES (the Netherlands Research Center for Integrated Solid Earth Science) who provided the computational resources.

References

Babeyko, A. Y. and Sobolev, S. V.: High-resolution numerical modelling of stress distribution in visco-elasto-plastic subducting slabs, Lithos, 103, 205–216, 2008.

Baes, M., Govers, R., and Wortel, R.: Subduction initiation along the inherited weakness zone at the edge of a slab: Insights from numerical models, Geophys. J. Int., 184, 991–1008, 2008.

Behounkova, M. and Cizkova, H.: Long-wavelength character of subducted slabs in the lower mantle, Earth Planet. Sci. Lett., 275, 43–53, 2010.

Billen, M. I. and Gurnis, M.: Comparison of dynamic flow models for the Central Aleutian and Tonga-Kermadec subduction zones, Geochem. Geophys, Geosyst, 4, 17 pp., doi:10.1029/2001GC000295, 2003.

Billen, M. I.: Slab dynamics in the transition zone, Phys. Earth Planet. Int., 25, 297–356, 2010.

Burgmann R. and Dresen G.: Rheology of the lower crust and upper mantle: evidence from rock mechanics, geodesy and field observations, Ann. Rev. Earth Planet. Sci., 36, 531–536, 2008.

Capitanio, F. A., Stegman, D. R., Moresi, L. N., and Sharples, W.: Upper plate controls on deep subduction,trench migration and deformations at convergent margins, Tectonophysics, 483, 80–92, 2010.

Cizkova, H., van den Berg, A. P., Spakman, W., and Matyska, C.: The viscosity of Earth's lower mantle inferred from sinking speed of subducted lithosphere, Phys. Earth Planet. Int., in press., 2012.

Cizkova, H., van Hunen, J., van den Berg, A. P.: Stress distribution within subducting slabs and their deformation in the transition zone, Phys. Earth Planet. Int., 161, 202–214, 2007.

Cristensen, U. R. and Yuen, D. A.: Layered convection indiced by phase transition, J. Geophys. Res., 99, 10291–10300, 1985.

Enns, A., Becker, T. W., and Schmeling, H.: The dynamics of subduction and trench migration for viscosity stratification, Geophys. J. Int., 160, 761–775, 2005.

Funiciello, F., Faccenna, C., Giardini, D., and Regenauer-Libeb, K.: Dynamics of retreating slabs: Insights from three-dimensional laboratory experiments, J. Geophys. Res., 108, 16 pp., doi:10.1029/2001JB000896, 2003.

Funiciello, F., Faccenna, C., Heuret, A., Lallemand, S., Giuseppe, E. Di., and Becker, T. W.: Trench migration, net rotation and slab-mantle coupling, Earth Planet. Sci. Lett., 271, 233–240, 2008.

Gerya, T.: Future directions in subduction modelling, J. Geodynam., 52, 344–378, 2011.

Han, L. and Gurnis, M.: How valid are dynamic models of subduction and convection when plate motion are prescribed? Physics of the Earth and planetary interiors, 110, 235–246, 1999.

Jadamec, M. A. and Billen, M. I.: Reconciling surface plate motions with rapid three-dimensional mantle flow around a slab edge, Nat. Lett., 465, 338–342, 2010.

Jadamec, M. A. and Billen, M. I.: The role of rheology and slab shape on rapid mantle flow: Three-dimensional numerical models of the Alaska slab edge, J. Geophys. Res., 117(B2), 20 pp., doi:10.1029/2011JB008563, 2012.

Karato, S., Rubie, D., and Hong Yan, S.: Dislocation recovery in olivine under deep upper mantle conditions: implication for creep and diffusion, J. Geophys. Res., 98, 9761–9768, 1993.

Karato, S., Riedel, M., and Yuen, D. A.: Rheological structure and deformation of subducted slabs in mantle transition zone: implications for mantle circulation and deep earthquakes, Phys. Earth Planet. Int., 127, 83–108, 2001.

Kaufmann, G. and Lambek, K.: Mantle dynamics, postglacial rebound and the radial viscosity profile, Phys. Earth Planet. Int., 121, 301–324, 2000.

Lithgow-Bertelloni, C. and Guynn, J. H.: Origin of the lithospheric stress field, J. Geophys. Res., 109, 32 pp., doi:10.1029/2003JB002467, 2004.

SED

4, 707–744, 2012

Manea, V. and Gurnis, M.: Subduction zone evolution and low-viscosity wedges and channels, Earth Planet. Sci. Lett., 264, 22-45, 2007.
Ozbench, M., Regenauer-Lieb, K., Stegman, D., Morra, G., Farrington, R., Hale, A., May, D. A., Freeman, J., Bourgouin, L., Muhlhaus, H., and Moresi, L.: A model comparison study of large-scale mantle-lithosphere dynamics driven by subduction, Phys. Earth Planet. Int., 171, 224–234, 2008.
Piromallo, C., Becker, T. W., Funiciello, F., and Faccenna, C.: Three-dimensional instantaneous mantle flow induced by subduction, Geophys. Res. Lett., 33, 4 pp., doi:10.1029/2005GL025390, 2006.
Quinquis, M., Buiter, S., and Ellis, S.: The role of boundary conditions in numerical models of subduction zone dynamics, Tectonophysics, 497, 57–70, 2011.
Quinteros, J., Sobolev, S. V., and Popov, A. A.: Viscosity in transition zone and lower mantle: Implication for slab penetration, Geophys. Res. Lett., 37, 5 pp., doi:10.1029/2010GL043140, 2010.
Schellart, W. P., Freeman, J., Stegman, D. R., Moresi, L., and May, D.: Evolution and diversity of subduction zones controlled by slab width, Nature, 446, 308–311, 2007.
Shellart, W. P., Stegman, D. R., and Freeman, J.: Global trench migration velocities and slab migration induced upper mantle volume fluxes: Constraints to find an Earth reference frame based on minimizing viscous dissipation, Earth Sci. Rev, 88, 118–144, 2008.
Schmeling, H., Babeyko, A., Enns, A., Faccena, C., Funiciello, F., Gerya, T., Golabek, G., Grigull, S., Kaus, B., Morra, G., Schmalholz, S. M., and van Hunen, J.: A benchmark omparison of spontaneous subduction models-towards a free surface, Phys. Earth Planet. Int., 171, 198–223, 2008.
Simmons, N. A., Forte, A. M., and Grand, S. P.: Constraining mantle flow with seismic and geodynamic data: a joint approach, Earth Planet. Sci. Lett., 246, 109–124, 2006.
Stegman, D. R., Schellart, W. P., and Freeman, J.: Competing influence of plate width and far-field boundary conditions on trench migration and morphology of subducted slabs in the upper mantle, Tectonophysics, 483, 46–57, 2010.
Turcotte D. L. and Schubert G.: Geodynamics, Cambridge University Press, 2002.
van den Berg, A. P., Yuen, D., and van Keken, P. E.: Efect of depth variations in creep laws on the formation of plates in mantle dynamics, Geophys. Res. Lett., 18, 2197–2200, 1991.
van Dinther, Y., Morra, G., Funiciello, F., and Faccena, C.: Role of the overriding plate in the subduction process: insights from numerocal models, Tetonophysics, 484, 74–86, 2010.

SED
4, 707–744, 2012

van Hunen, J.: Shallow and buoyant lithospheric subduction: causes and impliations from thermo-chemical numerical modelling, PhD thesis, Utrecht University, Utrecht, 2001.
van Hunen, J., van den Berg, A. P., and Vlaar, N. J.: A thermo-mechanical model of horizontal subduction below an overriding plate, Earth Planet. Sci. Lett., 182, 157–169, 2000.
van Hunen, J. and Allen, M. B.: Continental collision and slab break-off: A comparison of 3-D numerical models with observations, Earth Planet. Sci. Lett., 302, 27–37, 2011.

Table 1. Parameters of the model.

Symbol	Meaning	Value	Dimension
c_p	Specific heat	1250	$\mathrm{J\,kg^{-1}\,K^{-1}}$
k	Thermal conductivity	4.27	$\mathrm{Wm^{-1}\,K^{-1}}$
R	Gas constant	8.31	$\mathrm{J\,K^{-1}\,m^{-3}}$
Ra	Thermal Rayleigh number	1.7×10^7	–
t	Time:		
	slab initialization	3.5	My
	slab retreating	10–30	My
	Age of the lithosphere	40–100	My
T	Temperature	–	K
T_0	Surface temperature	273	K
δT	Vertical temperature contrast	1500	K
v_{subd}	Initial subduction velocity	10	$\mathrm{cm\,yr^{-1}}$
u	Velocity	–	$\mathrm{m\,s^{-1}}$
α	Thermal expansion coefficient	3×10^{-5}	$\mathrm{K^{-1}}$
ρ_0	Reference density	3413	$\mathrm{kg\,m^{-3}}$
h	Height of the model domain	1000	km
	Width of the domain	3000–5000	km
	Reference strainrate	10^{-18}	$\mathrm{s^{-1}}$
η	Reference viscosity	10^{21}	Pa s
κ	Thermal diffusivity	10^{-6}	$\mathrm{m^2\,s^{-1}}$
	Phase transition at 410 km:		
	clapeyron slope	4.1	$\mathrm{MPa\,K^{-1}}$
	density contrast	273	$\mathrm{kg\,m^{-3}}$
	Phase transition at 660 km:		
	clapeyron slope	–1.9	$\mathrm{MPa\,K^{-1}}$
	density contrast	342	$\mathrm{kg\,m^{-3}}$
	Viscosity of LVZ	10^{19}	Pa s
Γ_k	Phase function for kth phase	-	-
g	Gravitational acceleration	9.8	$\mathrm{m\,s^{-2}}$
P	Hydrostatic pressure	–	Pa
	Rheological parameters, wet olivine:		
A_{dif}	diffusion prefactor	5.310^{15}	$\mathrm{s^{-1}}$
A_{dis}	dislocation prefactor	2.010^{18}	$\mathrm{s^{-1}}$
b	Burgers vector	510^{-10}	m
d	grain size	110^{-3}	mm
m	grain size exponent	2.5	–
n	stress exponent dislocation creep	3	-
V	activation volume, diffusion creep	5	$\mathrm{cm^3\,mol^{-1}}$
V	activation volume, dislocation creep	10	$\mathrm{cm^3\,mol^{-1}}$
E	activation energy, diffusion creep	240	$\mathrm{KJ\,mol^{-1}}$
E	activation energy, dislocation creep	423	$\mathrm{KJ\,mol^{-1}}$
τ_{ij}	ijth component of the stress tensor	–	–
$\dot{\epsilon}$	ijth component of the strain rate	–	–
u_i	ith component of the velocity	–	–

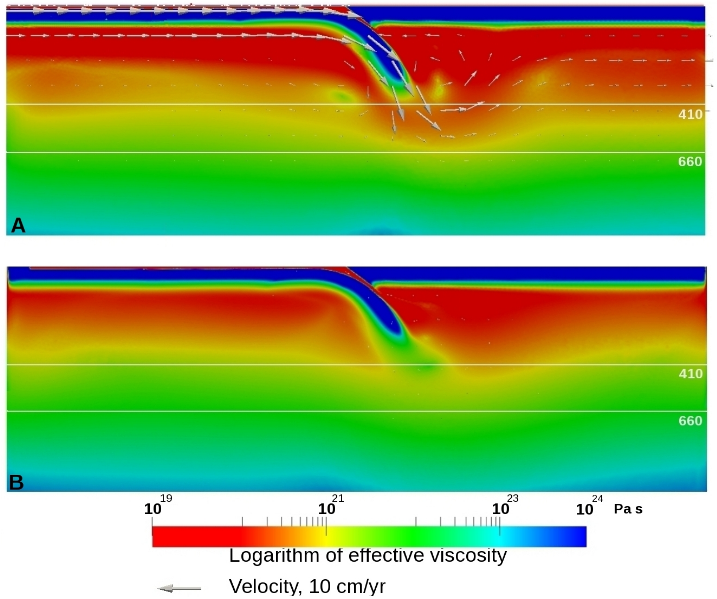

Fig. 1. The rheology and flow field after the initial 3.5 My of kinematically forced subduction consistent with: **(A)** open sidewalls, **(B)** closed sidewalls. The color scale shows 10-logarithm of effective viscosity. White lines corresponds to the approximate position of phase transition zones at 410 km and 660 km.

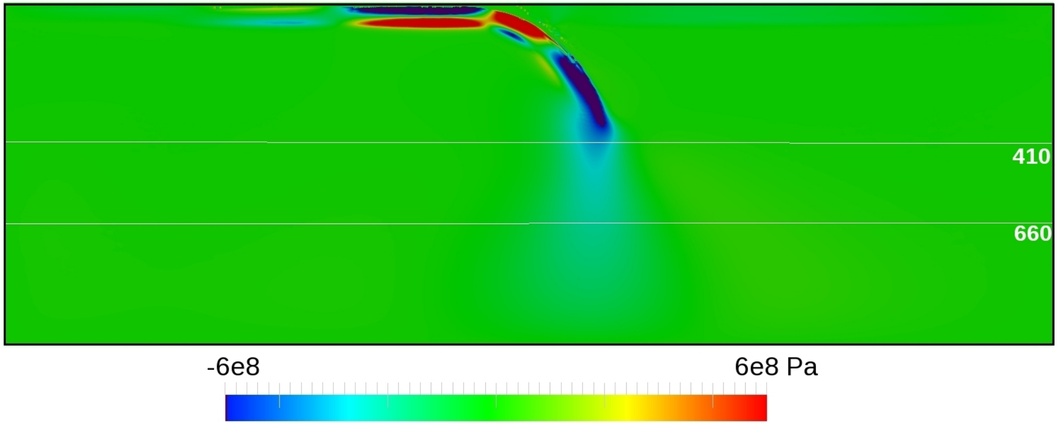

Fig. 2. Stress component τ_{22} for the initial model with open boundaries after 3.5 My of kinematically forced evolution (Fig. 1a). Note the down-dip compression in the slab.

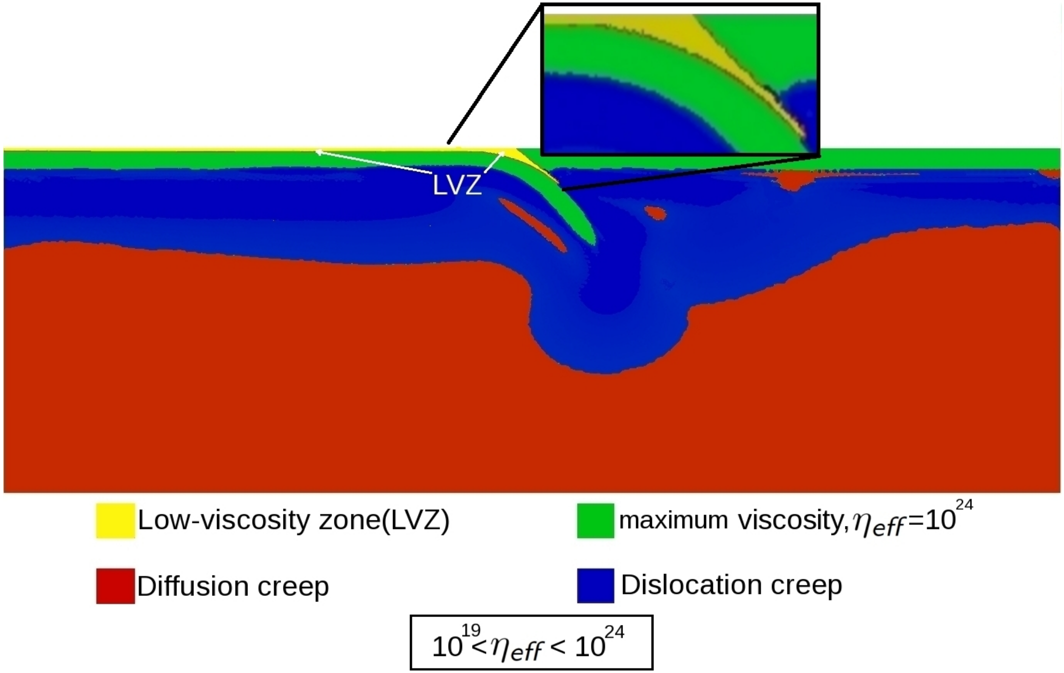

Fig. 3. Dominant deformation mechanism in the initial model with open side boundaries of Fig. 1a. Different colors correspond to regions where the individual deformation mechanism are dominant.

SED
4, 707–744, 2012

Using open sidewalls

M. Chertova et al.

SED
4, 707–744, 2012

Using open sidewalls

M. Chertova et al.

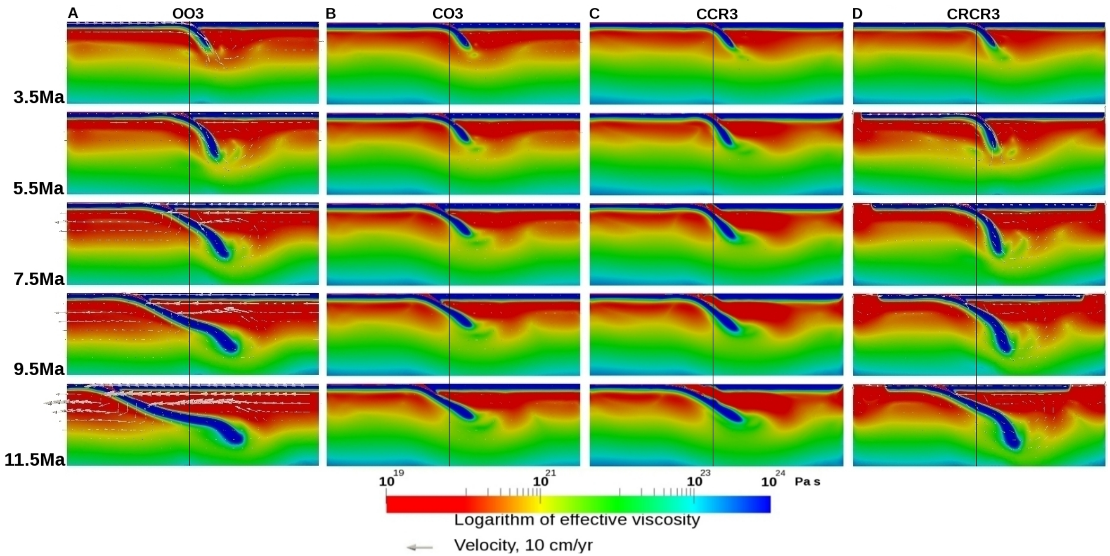

Fig. 4. Evolution of the subduction process for model OO3 with open boundaries, model CO_3 closed left and open right boundary, model CCR3 with closed right and left boundaries with "spreading center" on the right boundary and model CRCR3 with closed boundaries. Arrows show the direction and magnitude of flow field. Identical scaling of the velocity vectors applies to all cases.

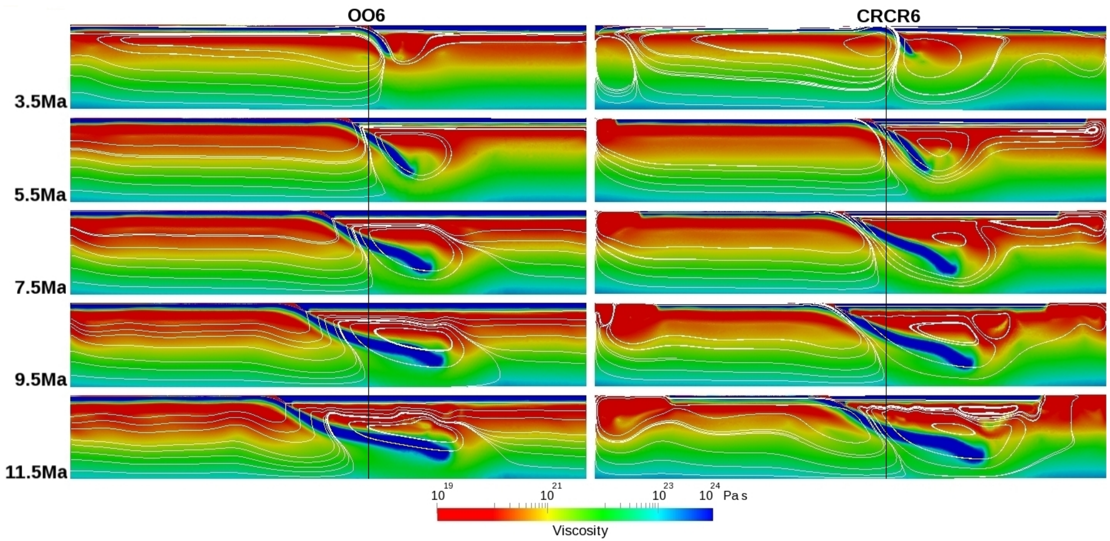

Fig. 5. Snapshots of the effective viscosity and flow pattern for 2 subduction models, on the right- model domain with ratio 6:1, closed boundaries (CRCR6), on the left- model domain with ratio 6:1, open boundaries (OO6).

SED
4, 707–744, 2012

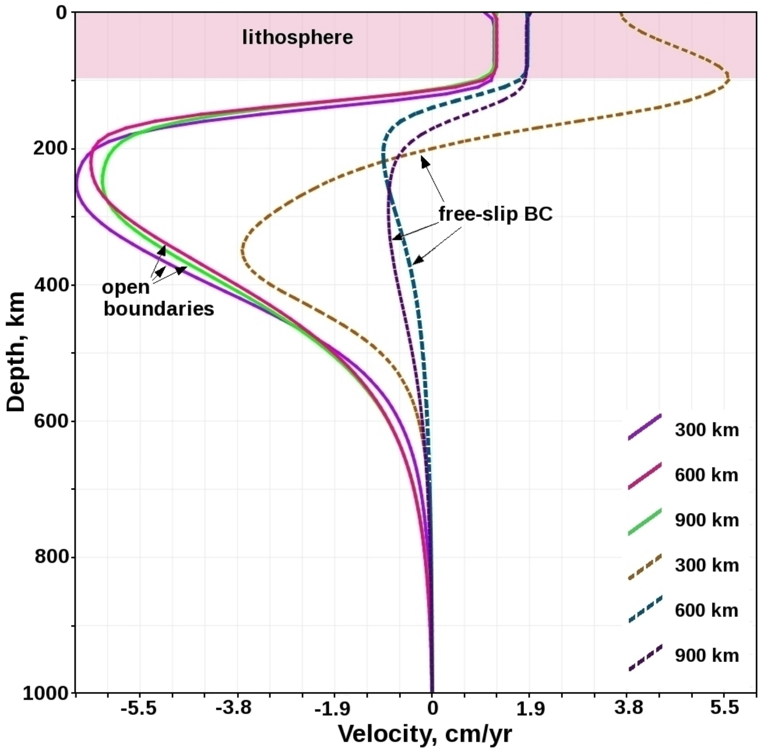

Fig. 6. Velocity profiles for the model with open boundaries, OO6 (solid lines) and model with closed boundaries, CRCR6 (dashed lines). Profiles were taken after 14 My from the beginning of the subduction process, distances from the left side of the model domain indicated in the legend.

SED
4, 707–744, 2012

Using open sidewalls

M. Chertova et al.

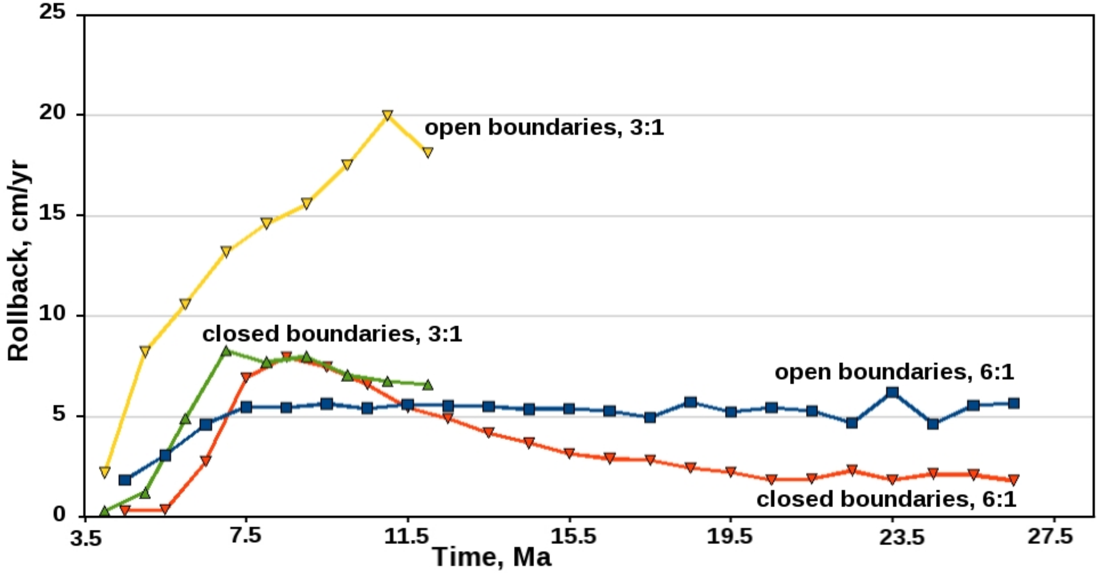

Fig. 7. Speed of rollback for the model with open boundaries and model with closed boundaries: model OO3 (yellow line), model CRCR3 (green line), model OO6 (blue line) and model CRCR6 (red line).

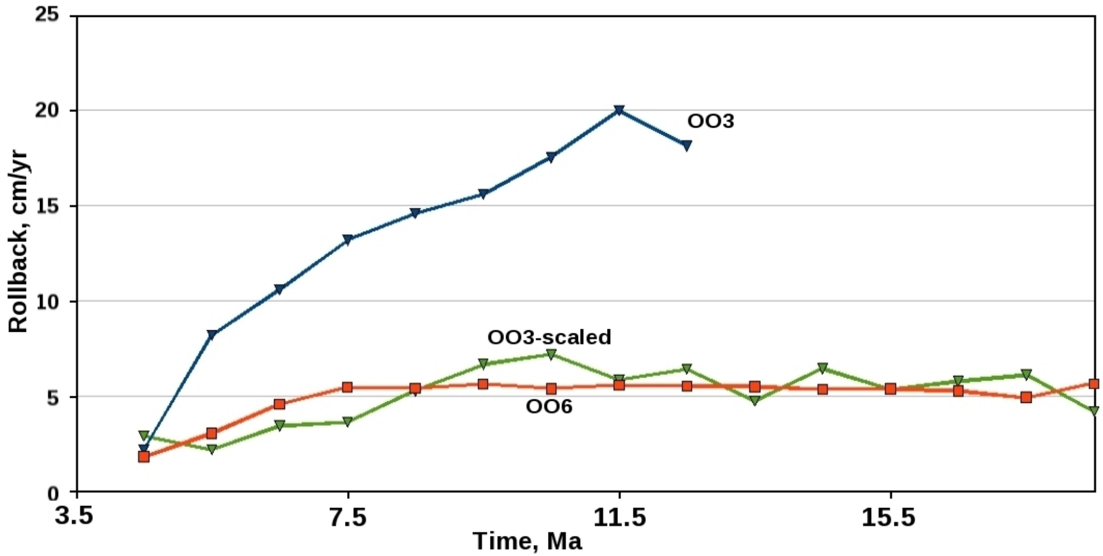

Fig. 8. Evolution of the speed of rollback for two models: model OO3 with aspect ratio 3:1 (blue line), and model OO6 with aspect ratio 6:1 (red line) and scaled speed of rollback for the model OO3 with aspect ratio 3:1 (green line).

SED
4, 707–744, 2012

Using open sidewalls

M. Chertova et al.

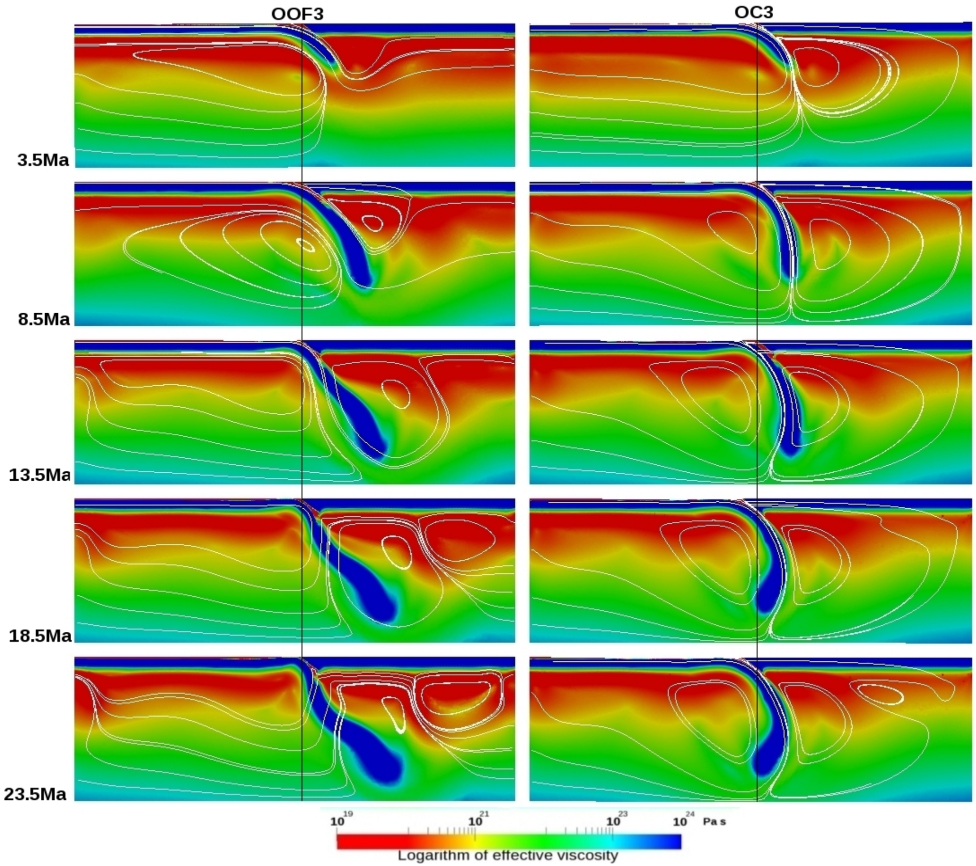

Fig. 9. Evolution of the subduction process for model OOF3 with open boundaries and fixed overriding plate (on the left) and model OC3 with closed right boundary (on the right). Arrows show the direction and magnitude of flow field.

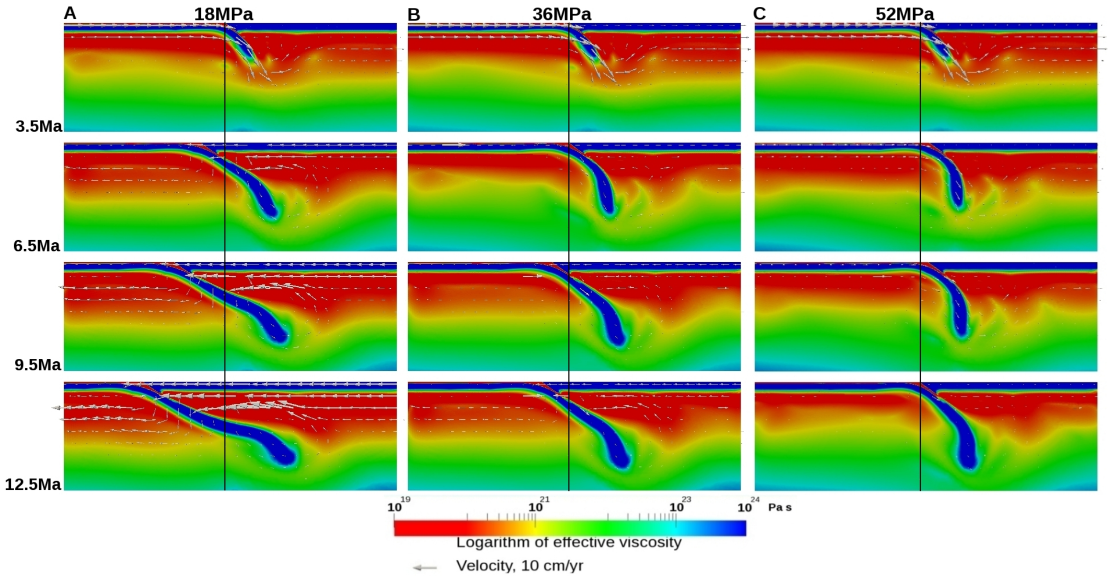

Fig. 10. The evolution of the models with open boundary conditions with different intra-plate stress values on the overriding plate: **(A)** model with "intra-plate" stress 18 MPa; **(B)** model with "intra-plate" stress 36 MPa; **(C)** model with "intra-plate" stress 52 MPa. Vertical black lines represent the initial trench position.

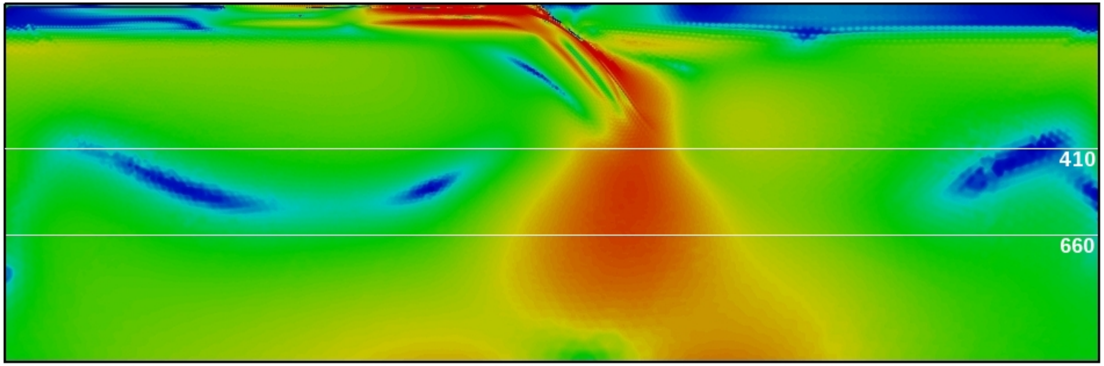

Fig. A1. Energy dissipation for the model with open boundaries and aspect ratio 3:1 at time = 3.5 My.

SED
4, 707–744, 2012

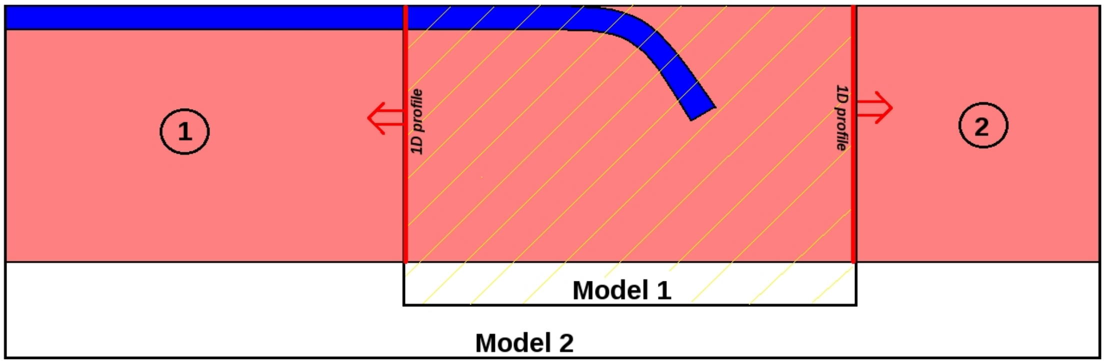

Fig. A2. Schematic representation of the subduction model. See text for the explanation.

SED
4, 707–744, 2012

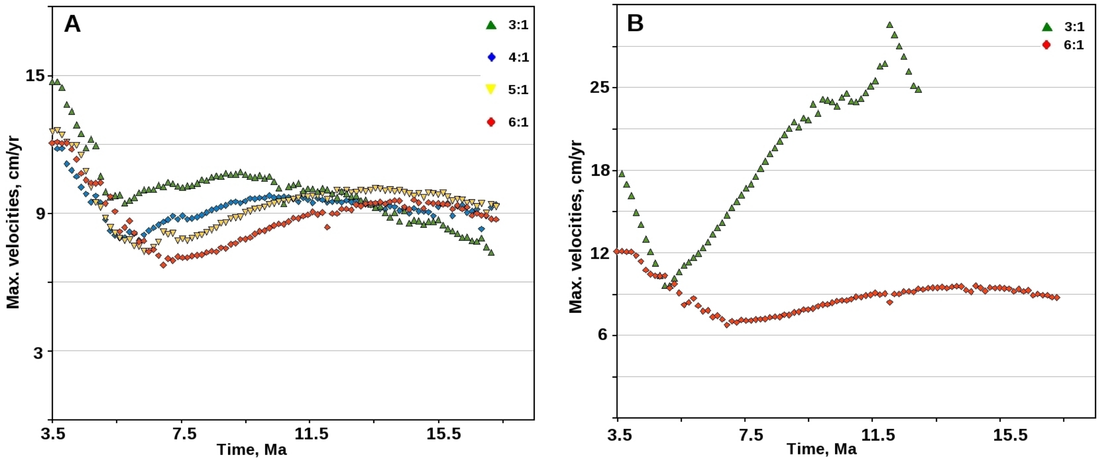

Fig. A3. Maximum velocities for model with aspect ratio 6:1, and scaled maximum velocities for models with 3:1, 4:1 and 5:1 aspect ratios. B. Comparison of maximum velocities for two models without applying the velocity scaling procedure.

SED
4, 707–744, 2012